

## Article

# Susceptible Plasmonic Photonic Crystal Fiber Sensor with Elliptical Air Holes and External-Flat Gold-Coated Surface

Chung-Ting Chou Chao <sup>1</sup>, Muhammad Raziq Rahimi Kooh <sup>2</sup> , Yuan-Fong Chou Chau <sup>2,\*</sup>   
and Roshan Thotagamuge <sup>3,\*</sup> 

<sup>1</sup> Department of Optoelectronics and Materials Technology, National Taiwan Ocean University, Keelung 20224, Taiwan

<sup>2</sup> Centre for Advanced Material and Energy Sciences, Universiti Brunei Darussalam, Tungku Link, Gadong BE1410, Brunei

<sup>3</sup> Department of Nano Science Technology, Faculty of Technology, Wayamba University of Sri Lanka, Kuliyaipitiya 60200, Sri Lanka

\* Correspondence: chou.fong@ubd.edu.bn (Y.-F.C.C.); roshan@wyb.ac.lk (R.T.)

**Abstract:** This paper proposes and analyzes a simple surface plasmon resonance (SPR)-based elliptical air hole photonic crystal fiber (PCF) sensor. The fiber structure comprises an analyte channel of the fiber surface coated with a gold layer on the flat surface and the fiber's external surface. Numerical simulations are conducted using the finite element method (FEM) with an external sensing approach. We found that the thickness of plasmonic material (Au) is the most crucial factor that affects the full width at half maximum (FWHM) and confinement loss amplitude. We also demonstrated that the proposed elliptical air hole SPR-PCF is superior to circular air hole SPR-PCF in terms of confinement loss and FWHM. According to the wavelength interrogation technique, the simulation results show that the designed SPR-PCF sensor can attain a maximum sensitivity of 116,500 nm/RIU and a resolution of  $8.58 \times 10^{-7}$  RIU (RIU: refractive index unit) for the analyte RI of 1.395. We believe the proposed SPR-PCF sensor can be a potential candidate for biomolecular and biological analyte detection.

**Keywords:** surface plasmon resonance; photonic crystal fiber; finite element method; refractive index sensitivity; resolution



Citation: Chou, C.-T.C.;

Kooh, M.R.R.; Chau, Y.-F.C.;

Thotagamuge, R. Susceptible

Plasmonic Photonic Crystal Fiber

Sensor with Elliptical Air Holes and

External-Flat Gold-Coated Surface.

*Photonics* **2022**, *9*, 916. [https://](https://doi.org/10.3390/photonics9120916)

[doi.org/10.3390/photonics9120916](https://doi.org/10.3390/photonics9120916)

Received: 5 November 2022

Accepted: 25 November 2022

Published: 29 November 2022

**Publisher's Note:** MDPI stays neutral with regard to jurisdictional claims in published maps and institutional affiliations.



**Copyright:** © 2022 by the authors. Licensee MDPI, Basel, Switzerland. This article is an open access article distributed under the terms and conditions of the Creative Commons Attribution (CC BY) license (<https://creativecommons.org/licenses/by/4.0/>).

## 1. Introduction

The effects of surface plasmon resonance (SPR) on the surface of nanometals and dielectrics have attracted researchers' attention because of the unique optic properties and the potential to overcome the diffraction limit in the nanoscale region [1–4]. SPR refers to the coherent oscillations of conduction electrons on the surface of a plasmonic material, resulting in localized SPRs and traveling surface plasmon polaritons (SPPs) [5,6]; these are popular optical devices for sensing and detecting applications [7–9].

SPR biosensing and gas detection using prism coupling was first proposed in 1983 [10]. In 1993, Jorgenson first presented the SPR optical fiber sensor and claimed that the designed sensor had the highest resolution, at  $7.5 \times 10^{-4}$  RIU [11]. Since then, many research groups have developed various optic fiber SPR sensors for chemical and biochemical sensing, such as Mach-Zehnder interferometer fiber [12], side-polishing technique fiber [13], graphene-deposited fiber [14], air-core hole SPR fiber [15], D-shaped optical fiber [16,17], photonic crystal fiber (PCF) [18,19], and Bragg grating SPR fiber [20,21] sensors. In the past decades, concerning the controllability of coupling between core-guided and SPP modes, attention has been focused on the PCF-based SPR sensor (SPR-PCF hereafter). Plasmonic materials and PCF technology are combined to construct an SPR-PCF-based sensor, providing design flexibility and minor size requirements [22–25].

The mechanism of an SPR-PCF sensor operates using transient electromagnetic (EM) wave interaction with the plasmonic materials (e.g., gold (Au), silver (Ag), copper (Cu), etc.). The EM waves can penetrate through the fiber cladding region and generate an evanescent EM wave. This then excites the free electrons of the nanometal surface and produces an SPP wave at the interface of the metal and dielectric [26–30]. At a resonance wavelength, the real part of the effective RI of the core-guided mode and SPP mode is completely phase-matched. It generates a pointy confinement loss peak, which can inspect the unknown sample/analyte [31–33].

The SPR-PCF-based sensors can categorize internal and external sensing schemes [26,34,35]. For the internal sensing approach, it can be challenging to process metal coating and liquid dropping in the inside structure of fiber [36,37]. The external sensing method can easily detect the unknown analyte by infiltrating the analyte through the metal surface. Therefore, the external sensing method is well known, since the practical realization is easy and possible [17,38].

The external sensing method for SPR-PCF-based sensors has become a central topic of interest in recent years. Kiroriwal et al. proposed an SPR-PCF refractive index (RI) sensor with 36 air holes and obtained a wavelength sensitivity of 8000 nm/RIU in the RI range of 1.36–1.40 [39]. Popescu et al. demonstrated a honeycomb SPR-PCF sensor with two complementary supermodes [23]. They claimed that the sensitivity can increase from 1000 nm/RIU to 4500 nm/RIU. Shakya et al. investigated a tetra-core-based SPR-PCF sensor containing three different dimensions of air holes [40] and obtained a wavelength sensitivity of 5000 nm/RIU. Kumar et al. verified a D-shape SPR-PCF sensor using Mxene/Au material thin film. They obtained a wavelength sensitivity of 7000 nm/RIU and 13,000 nm/RIU for the Mxene layer thicknesses of 14 nm and 27 nm, respectively [41]. Paul et al. presented a dual-core SPR-PCF sensor [42] and obtained a maximum wavelength sensitivity of 25,000 nm/RIU, with an analyte RI of 1.38. Tong et al. displayed a three-core SPR-PCF sensor with an outer layer of Au film [24]. Introducing the multi-core in the fiber structure can improve the sensor performance. Zhao et al. illustrated the photonic bandgap fiber and the Bragg fiber with various forms, including fuse-tapered fiber structure, D-type fiber structure, and cladding-off fiber structure [43]. They fabricated the proposed structures and confirmed that the designed devices have the merits of high sensitivity and resolution.

All of the abovementioned SPR-PCF sensors have high wavelength sensitivity. However, the proposed SPR-PCF structures possess many air holes in the PCF cladding (more than 20), which results in a complex fabrication. In this work, we propose a simple SPR-PCF sensor structure with eight elliptical air holes and a fiber surface coated with an Au layer on the polished surface and external fiber surface. The proposed SPR-PCF sensor can detect an analyte externally. We investigate the sensing performance of the proposed device employing the finite element method (FEM)-based COMSOL Multiphysics software. We consider the effects of RI surrounding the fiber structure, the thickness of Au film, and the ratio of semi-minor and semi-major axes of elliptical air holes to ensure accuracy. The results offer an experimental basis and theoretical guidance for designing high-sensitivity SPR-PCF sensors.

This paper organizes as follows: Section 1 is the introduction. Section 2 presents the numerical modeling method and basic formulas. The optimization of the structural parameters is discussed in detail in Section 3. Section 4 concerns the application as a RI SPR-PCF sensor and compares this work with similarly reported studies. Finally, the results are summarized in the concluding section.

## 2. Numerical Modeling Method and Basic Formulas

For the fiber structure's simplicity, the number of air holes chosen is as low as possible. We decided on eight elliptical holes with three different sizes in our design, based on the FEM simulations. Figure 1 depicts the cross-section of the designed SPR-PCF-based sensor, with eight elliptical air holes in the PCF's cladding. The semi-major axis of different

sizes of elliptic air-holes are  $a_{1y}$ ,  $a_{2y}$ , and  $a_{3y}$ , and their coordinates are  $(\pm d_1, 0)$  for the biggest ones,  $(0, \pm d_2)$  for the middle size ones, and  $(\pm d_3, \pm d_2)$  for the smallest size ones, correspondingly. The  $d_1$ ,  $d_2$ , and  $d_3$  are fixed at  $1.8 \mu\text{m}$ ,  $1.5 \mu\text{m}$ , and  $1.5 \mu\text{m}$  throughout this work. The purpose of using diverse sizes of elliptical air holes is to generate a higher birefringence [44–47]. Their sensing performance is superior to a circular one. The ratio of semi-minor and semi-major axes (i.e., ellipticity,  $e$ ) is  $e = a_{1x}/a_{1y} = a_{2x}/a_{2y} = a_{3x}/a_{3y}$ . The distance between the top elliptical air hole and the polished surface is  $h$ .

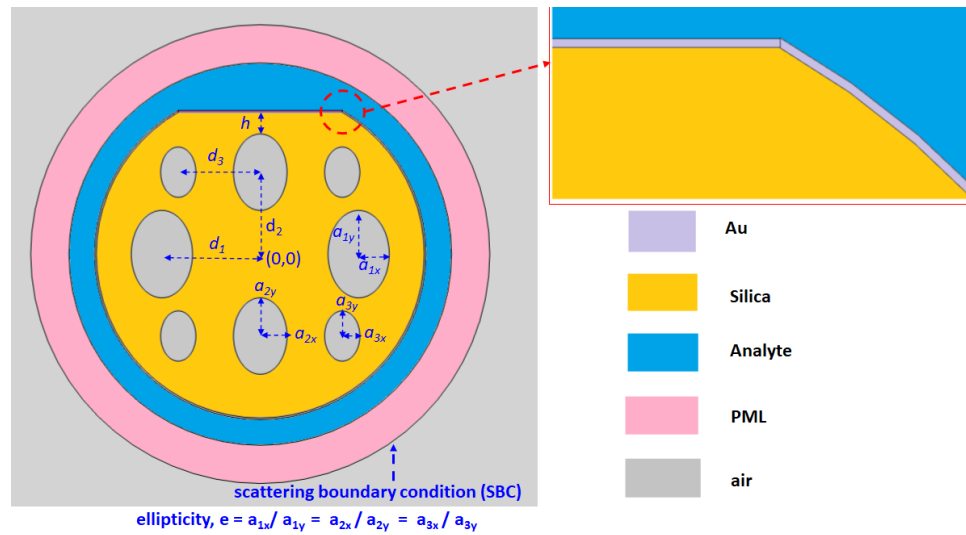


**Figure 1.** Cross-section of the designed SPR-PCF sensor with structural parameters.

The Au film is covered on the top cutting flat plane and the outer surface of the SPR-PCF sensor with a thickness of  $t_{Au}$ , which facilitates the detection ability of the proposed PCF sensor. The analyte layer with a thickness of  $0.5 \mu\text{m}$  is located on the Au layer’s outer surface to sense the surrounding medium. The maximum mesh element sizes are set as the corresponding thickness layer in the Au layer. The analyte surrounds the entire SPR-PCF structure and is a liquid with different RIs in RI sensing. A change in the resonant wavelength ( $\lambda_{res}$ ) occurs when the analyte’s RI changes, allowing us to detect changes in RI. We numerically investigated the proposed PCF sensor using the full vectorial FEM-based software COMSOL Multiphysics to optimize structural parameters and determine the sensor sensitivity and selectivity. A circular perfectly matched layer (PML) boundary condition with a thickness of  $0.7 \mu\text{m}$  and a scattering boundary condition (SBC) were added to the outer computational domain to absorb the artificial back-reflection at the boundaries during the simulation. In the FEM simulations, we utilized the finer meshing elements of 17,956 domain elements and 1453 boundary elements.

The core and cladding regions are fused silica with a diameter of the silica layer of  $6 \mu\text{m}$ . The RI of silica is obtained from the Sellmeier Equation [48]:

$$n^2(\lambda) = 1 + \frac{B_1\lambda^2}{\lambda^2 - C_1} + \frac{B_2\lambda^2}{\lambda^2 - C_2} + \frac{B_3\lambda^2}{\lambda^2 - C_3} \quad (1)$$

where  $n$  and  $\lambda$  denote the wavelength-dependent RI and wavelength (in  $\mu\text{m}$ );  $B_1, B_2, B_3, C_1, C_2,$  and  $C_3$  are the constant values of the Sellmeier Equation, which are listed in Table 1.

**Table 1.** The constant values of the Sellmeier Equation.

$B_1$	$B_2$	$B_3$	$C_1$	$C_2$	$C_3$
0.696163	0.4079426	0.897479400	0.0046791486	0.0135120631	97.9340025

The SPR-PCF sensing performance closely relies on the noble nanometal. Ag and Au are commonly utilized for plasmonic sensing applications. The Ag can offer a sharper SPR peak, but it possesses the drawbacks of being chemically unstable and easily oxidized [13]. Therefore, we used Au as the plasmonic material since it is chemically stable in an aqueous environment and displays a sizeable  $\lambda_{res}$  shift compared with other novel nanometals. The permittivity of Au is wavelength dependent and can be obtained from the Drude-Lorentz model [49,50]:

$$\epsilon_{Au} = \epsilon_{\infty} - \frac{\omega^2 D}{\omega(\omega + j\gamma_D)} - \frac{\Delta\epsilon\Gamma_L^2}{j\Gamma_L\omega + (\omega^2 - \Gamma_L^2)} \tag{2}$$

where the value of  $\epsilon_{\infty}$  (the permittivity of high frequency),  $\omega$  (angular frequency),  $\omega_D$  (plasmon resonance frequency),  $\gamma_D$  (damping frequency),  $\Omega_L$  (oscillation strength of the Lorentz oscillators), and  $\Gamma_L/2\pi$  (spectrum width) are listed in Table 2.

**Table 2.** The constant values of Equation (2).

$\epsilon_{\infty}$	$\omega$	$\omega_D/2\pi$	$\gamma_D/2\pi$	$\Omega_L$	$\Gamma_L/2\pi$
5.9673	$2\pi c/\lambda$	2113.6 THz	15.9 THz	650.07 THz	104.86 THz

The confinement loss (CL) spectrum of the core-guided mode can evaluate the sensing performance, and the CL of the core-guided mode can be described as follows [51,52]:

$$\alpha \cong 8.686 \times \frac{2\pi}{\lambda} \times Im[n_{eff}] \times 10^4 \frac{dB}{cm} \tag{3}$$

where  $Im(n_{eff})$  is an imaginary part of the effective RI of the core-guided mode.

Sensitivity is obtained by

$$S_A(\lambda)[nm/RIU] = \Delta\lambda_{peak}/\Delta n_{ana} \tag{4}$$

where  $\Delta\lambda_{peak}$  is the change in peak wavelength, and  $\Delta n_{ana}$  denotes the shift in two successive RIs.

Sensor resolution can be expressed by [28]

$$R[RIU] = n_{ana} \times \frac{\Delta\lambda_{min}}{\Delta\lambda_{peak}} \tag{5}$$

where  $\Delta\lambda_{min}$  is the wavelength resolution.

$L$  indicates the length of the sensor in cm (i.e., how long the sensor is for the specific RI), which can be computed as follows [29]:

$$L = \frac{1}{\alpha(\lambda, n_{ana})} \tag{6}$$

where  $\alpha(\lambda, n_{ana})$  is the overall CL for a particular wavelength.

The proposed SPR-PCF sensor can be fabricated with nanofabrication technology. To manufacture the proposed SPR-PCF sensor, PCF may utilize stack and drawing, extrusion, or capillary stacking techniques to make the prefabricated rod [53]. To adjust the air holes' size and obtain the elliptical air hole, the thin walls of the air holes are squeezed by controlling the pressure to obtain the ellipse [54]. In this manner, the proposed SPR-PCF can be fabricated successfully. Au can be deposited on the surface of the SPR-PCF by customized vapor deposition (CVD) or atomic layer deposition (ALD) [55] and exterior vapor deposition (EVD) [56]. However, this work focuses on something other than the fabrication procedures. As an alternative, several potential articles that investigated in-depth fabrication of the elliptical air holes in PCF are suggested [57–59].

### 3. Optimization of the Structural Parameters

The initial values of the geometrical parameters of the designed SPR-PCF structure are specified in Table 3.

**Table 3.** Initial geometrical parameters of the designed SPR-PCF.

$a_{1x}$ ( $\mu\text{m}$ )	$a_{1y}$ ( $\mu\text{m}$ )	$a_{2x}$ ( $\mu\text{m}$ )	$a_{2y}$ ( $\mu\text{m}$ )	$a_{3x}$ ( $\mu\text{m}$ )	$a_{3y}$ ( $\mu\text{m}$ )	$e$	$t_{Au}$ (nm)	$h$ ( $\mu\text{m}$ )	$n_{ana}$
0.8e	0.8	0.7e	0.7	0.2e	0.4	0.6	30	0.4	1.38

Note:  $e$  is ellipticity.

The real parts of the effective RIs of the core-guided mode (red dashed line) and SPP modes (black dashed line) and the CL spectrum of the core-guided mode (blue curve) in the proposed SPR-PCF sensor are shown in Figure 2, where the geometrical parameters of the PCF are as specified in Table 3. Figure 3a,b are the E-field distributions of the SPP and core-guided modes (y-polarization) at  $\lambda_{peak} = 694$  nm. In Figure 2, the  $\lambda_{peak}$  happens when the line of effective RIs of the core-guided mode overlaps with a high-order SPP mode. In this situation, the energy can transfer from the core-guided mode to the SPP mode, resulting in the CL peak of 79.92 dB/cm, which can be acquired at  $\lambda_{peak} = 694$  nm for  $n_{ana} = 1.38$ . Note that the SPR effect of SPP mode (see Figure 3a) on the top-flat surface of Au film is higher than that of the side-throw surface.

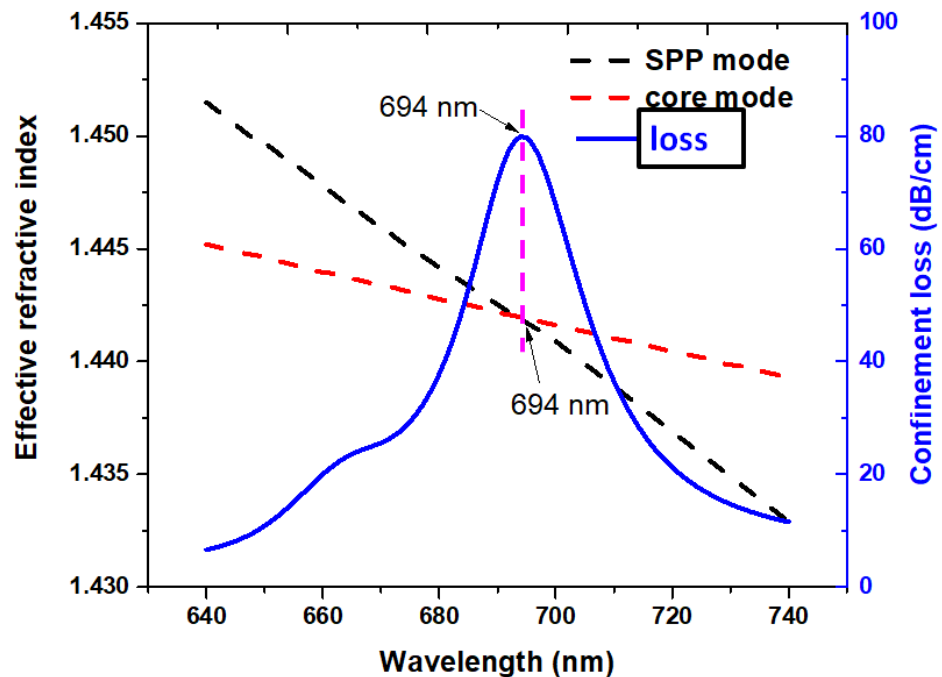


**Figure 2.** Real parts of the effective RIs of the core-guided mode (red dashed line) and SPP mode (black dashed line), and the confinement loss (CL) of core-guided mode (blue curve).

The geometrical parameters, such as the Au thickness ( $t_{Au}$ ), semi-major axes ( $a_{1y}$ ,  $a_{2y}$ , and  $a_{3y}$ ), ellipticity ( $e$ ), and the distance between the top elliptical air hole and the polished surface ( $h$ ), are the pivotal factors that can effectively affect the sensing performance of the designed device. In the following simulations, we change one of the geometrical parameters while fixing the other parameters specified in Table 3.

The thickness of coated plasmonic material,  $t_{Au}$ , has a potential impact on the CL of the SPR-PCF sensor. The  $t_{Au}$  strongly influences the  $\lambda_{peak}$  shift, which can be used in measuring the testing medium interaction with the surface of the Au layer. When the  $t_{Au}$  increases from 10 to 50 nm, which is comparable with the skin depth of the Au in the visible wavelength range [60]. Figure 4 shows the CL spectra of the core-guided mode

for various  $t_{Au}$ , ranging in  $10 \text{ nm} \leq t_{Au} \leq 50 \text{ nm}$ . As seen, the CL peak redshifts with the increase of  $t_{Au}$  from  $\lambda_{peak} = 498 \text{ nm}$  to  $\lambda_{peak} = 821 \text{ nm}$  when  $10 \text{ nm} \leq t_{Au} \leq 50 \text{ nm}$ . When the  $t_{Au}$  is relatively thin (e.g.,  $t_{Au} = 10, 15, 20,$  and  $25 \text{ nm}$ ), the energy of the evanescent EM wave on the Au surface is also weak. When the  $t_{Au}$  increases, the coupling effect between the core-guided mode and the SPP mode can be enhanced and reach the highest value of  $\lambda_{peak} = 694 \text{ nm}$  when  $t_{Au} = 30 \text{ nm}$ . The loss increases from  $3.18 \text{ dB/cm}$  to  $79.92 \text{ dB/cm}$  when  $t_{Au}$  changes from  $10 \text{ nm}$  to  $30 \text{ nm}$ . A thicker  $t_{Au}$  (e.g.,  $t_{Au} = 35, 40,$  and  $50 \text{ nm}$ ) mitigates the coupling effect between the core-guided mode and the SPP mode due to the shielding of the EM wave from the core region to the outer Au surface, leading to the decrease of the CL peak. As a result, the CL peak drops from  $79.92 \text{ dB/cm}$  to  $41.02 \text{ dB/cm}$  when  $t_{Au}$  is  $30 \text{ nm} \leq t_{Au} \leq 50 \text{ nm}$ . From Figure 4, we can conclude that the  $t_{Au}$  is the most crucial factor that affects the full width at half maximum (FWHM) and the amplitude of the CL peak. One can explain the matching impedance and SPR resonance conditions between the core region and the Au surface. The variation of  $t_{Au}$  results in impedance when the resonance condition of the fiber is satisfied.

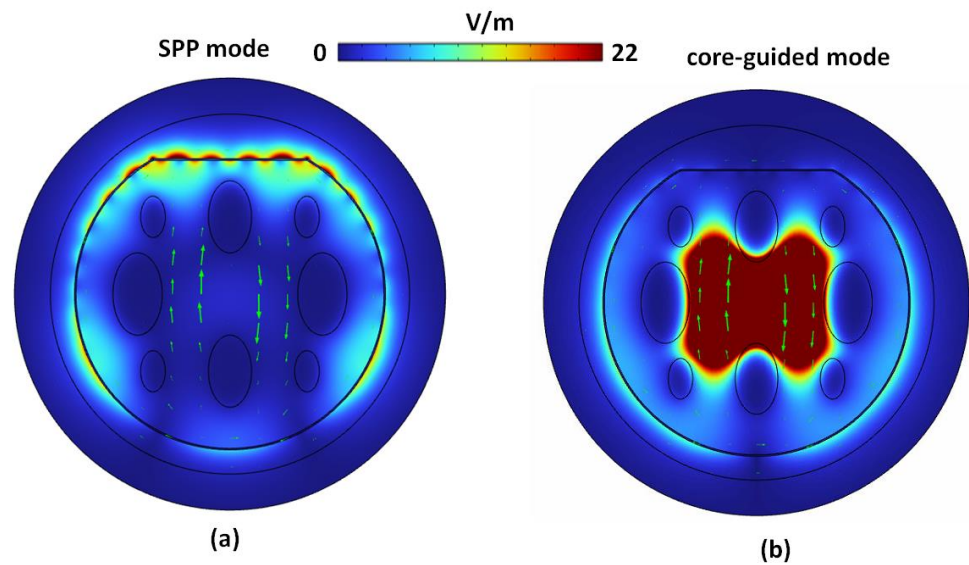
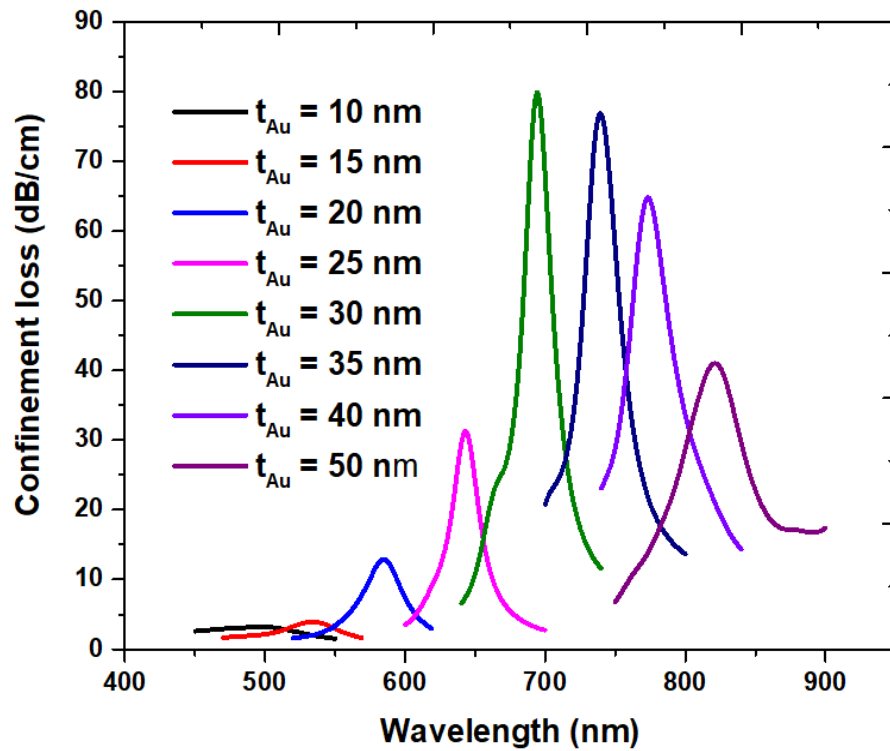


Figure 3. E-field distributions of the (a) SPP mode and (b) core-guided mode (y-polarized).

Meanwhile,  $\lambda_{peak}$  should increase to guarantee the impedance between the fiber core region and Au surface when the resonance condition of the fiber is changed by  $t_{Au}$ . It is noticeable that there is a sharp transition in the CL value when  $t_{Au}$  is increased from  $25$  to  $30 \text{ nm}$ . The reason can be understood from the resonance condition between the core-guided and SPP modes at various  $t_{Au}$ . This indicates that the highest energy exchange between guided and SPP modes occurs when  $t_{Au} = 30 \text{ nm}$ .

The size of the major axis in the elliptical air holes is essential in affecting the CL. Based on the FEM simulations, the major axis of the elliptical air holes, i.e.,  $a_{1y}$ ,  $a_{2y}$ , and  $a_{3y}$ , can significantly affect the coupling effect between the core-guided mode and SPP mode. Figures 5–7 display the CL versus wavelength for  $a_{1y} = (0.60, 0.65, 0.70, 0.75, 0.80, 0.85, 0.9) \mu\text{m}$ ,  $a_{2y} = (0.68, 0.70, 0.72, 0.74, 0.76, 0.78) \mu\text{m}$ , and  $a_{3y} = (0.35, 0.36, 0.37, 0.38, 0.39, 0.40, 0.41, 0.42) \mu\text{m}$ , respectively. The increase in CL indicates the nature of the coupling effect, and a higher CL can facilitate the energy transformation from the core-guided to the SPP mode. As observed in Figure 5, the CL peak occurs at  $\lambda_{peak} = 695 \text{ nm}$  for all cases except that of  $a_{1y} = 0.6 \mu\text{m}$ . The case of  $a_{1y} = 0.65 \mu\text{m}$  shows the highest CL peak of  $261.01 \text{ dB/cm}$  but reveals a larger FWHM of  $30 \text{ nm}$ . In contrast, a smaller CL peak for the cases of  $a_{1y} = 0.75, 0.80, 0.85,$  and  $0.9 \mu\text{m}$  are  $111.33, 79.92, 63.49,$  and  $55.97 \text{ dB/cm}$ , correspondingly. It is noticeable that the CL spectrum curve of  $a_{1y} = 0.60 \mu\text{m}$  displays a broad range of peak values. A larger FWHM (around  $60 \text{ nm}$ ) negatively influences the sensing performance.

Therefore, the best result is  $a_{1y} = 0.7 \mu\text{m}$  based on a CL value of 166.69 dB/cm and FWHM width of 20 nm.



**Figure 4.** Confinement loss spectra of the core-guided mode for various Au thicknesses,  $t_{Au} = (10, 15, 20, 25, 30, 35, 40, 50)$  nm.

In Figure 6, the CL peak redshifts and has a higher value with the increasing  $a_{2y}$  range being  $a_{2y} = (0.68, 0.70, 0.72, 0.74, 0.76, 0.78) \mu\text{m}$ . These values of  $a_{2y}$  are available in the proposed SPR-PCF and imply that we can manipulate the desired operation wavelength by varying the  $a_{2y}$ . In this case, we choose  $a_{2y} = 0.78 \mu\text{m}$  as an optimal value due to its higher CL value of 93.67 dB/cm and an acceptable FWHM of 20 nm. It can be seen in Figure 7 that the CL peaks exhibit a slight blueshift from  $\lambda_{peak} = 697 \text{ nm}$  to  $\lambda_{peak} = 693 \text{ nm}$ , and the CL values drop from 159.82 dB/cm to 59.01 dB/cm when  $a_{3y}$  varies in the range of  $a_{3y} = (0.35, 0.36, 0.37, 0.38, 0.39, 0.40, 0.41, 0.42) \mu\text{m}$ . The smaller  $a_{3y}$  experiences a higher CL value because the scaled-down  $a_{3y}$  facilitates driving the EM wave away from the PCF core region to the PCF surface. Note that in the structure optimization process, the change of  $a_{2y}$  will cause the CL peak to show a regular  $\lambda_{peak}$  shift and an increased CL value, while  $a_{1y}$  and  $a_{3y}$  only affect the CL value. The CL value depends on the contribution of the coupling effect from the core-guided mode to the SPP mode, and the  $\lambda_{peak}$  shift is related to the resonance condition and the variation of  $Im(n_{eff})$  in the SPR-PCF. As seen in Figure 6, one can obtain the desired working wavelength by changing the size of  $a_{2y}$ .

The ellipticity of elliptical air holes can remarkably affect the light energy coupling between the core-guided and SPP mode [19]. Figure 8 displays the CL versus wavelength for ellipticity  $e = 0.4, 0.5, 0.55, 0.60, 0.65, 0.70, 0.75,$  and 1.00. It is evident in Figure 8 that the CL redshifts from 688, 691, 693, 694, 698, 702, to 703 nm when the ellipticity increases from 0.4 to 1.00, while the intensity of CL and the width of FWHM decreases from (CL, FWHM) = (235.66 dB/cm, 25 nm), (137.14 dB/cm, 22 nm), (104.80 dB/cm, 20 nm), (79.92 dB/cm, 20 nm), (60.39 dB/cm, 19 nm), (44.99 dB/cm, 18 nm), (32.46 dB/cm, 17 nm) to (2.73 dB/cm, 60 nm). Compared to the elliptical air-hole cases, the circular air-hole case (i.e.,  $e = 1.00$ ) shows a lower amplitude of CL peak and a broadened FWHM. These results demonstrate that the elliptical air holes in the designed SPR-PCF sensor are superior to the case of circular air holes in terms of the CL and FWHM. The smaller ellipticity can facilitate

the energy transformation from the core-guided to the SPP mode. However, the smaller ellipticity will exhibit a larger FWHM, as observed in the dashed arrow lines in Figure 9. As a result, we choose the optimal value of  $e = 0.55$  in the viewpoint of the CL value and the width of FWHM (CL = 104.80 dB/cm, FWHM = 19 nm).

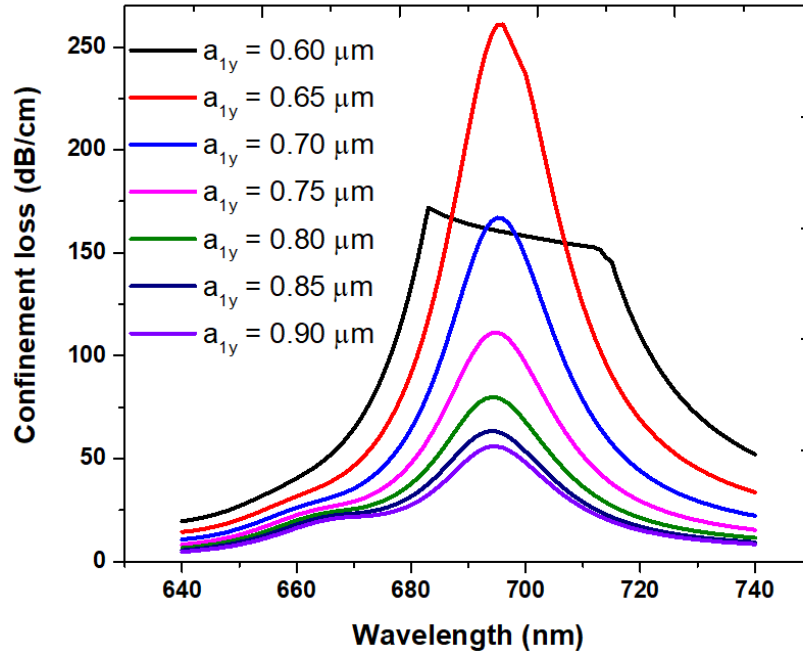


Figure 5. Confinement loss spectra of the core-guided mode for  $a_{1y} = (0.60, 0.65, 0.70, 0.75, 0.80, 0.85, 0.90) \mu\text{m}$ .

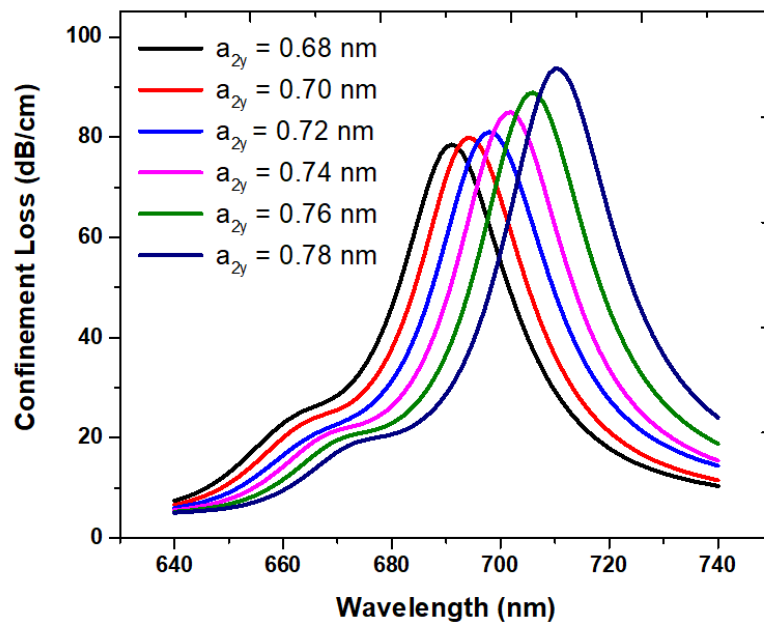


Figure 6. Confinement loss spectra of the core-guided mode for  $a_{2y} = (0.68, 0.70, 0.72, 0.74, 0.76, 0.78) \mu\text{m}$ .

Subsequently, we inspected the distance between the top elliptical air hole and the flat surface,  $h$ . As illustrated in Figure 9, the CL amplitude decreases with the increasing  $h$ . When  $h$  increases from 0 to  $0.6 \mu\text{m}$  in the step of  $0.1 \mu\text{m}$ , there is a slight blueshift from  $\lambda_{peak} = 695 \text{ nm}$  to  $\lambda_{peak} = 692 \text{ nm}$ , and the CL amplitude decreases from  $110.76 \text{ dB/cm}$  to  $69.29 \text{ dB/cm}$ . According to the CL spectrum, as shown in Figure 9, the available range

of  $h$  in the proposed structure can be selected as  $0 \mu\text{m} \leq h \leq 0.6 \mu\text{m}$ . The Au-coated flat surface can facilitate the coupling effect between the SPP wave and analyte, and the length of the Au-coated flat surface depends on different sizes of  $h$  value. Note that if  $h = 0 \mu\text{m}$ , the proposed SPR-PCF structure exhibits a circular outer surface (i.e., no flat surface), the CL amplitude can reach the highest value but shows a bigger FWHM (25 nm) and an unsmooth CL curve range of  $640 \text{ nm} \leq \lambda \leq 680 \text{ nm}$ . As a result, we selected  $h = 0.4 \text{ m}$  for the following simulation in terms of a smooth CL curve and a smaller FWHM (18 nm).

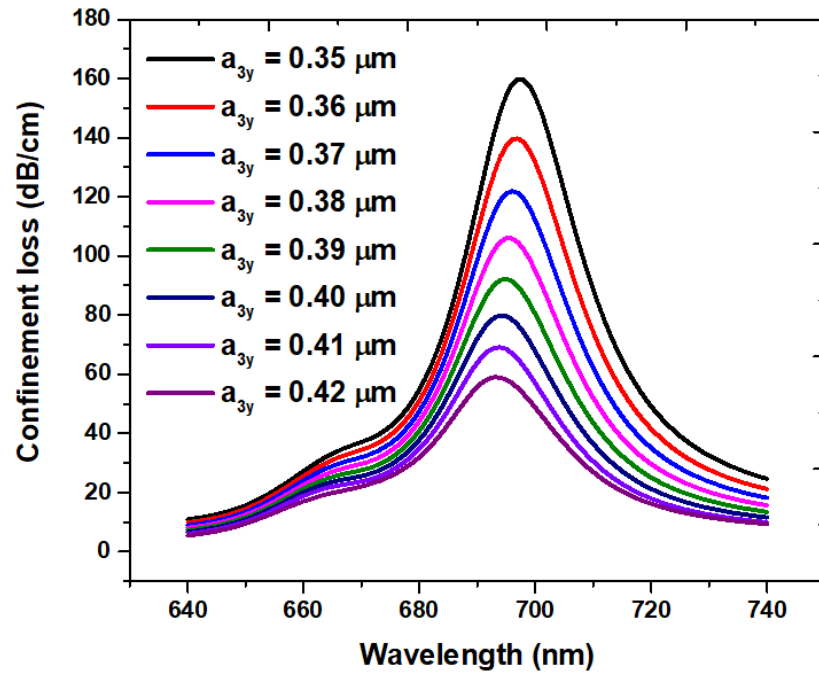


Figure 7. Confinement loss spectra of the core-guided mode for  $a_{3y} = (0.35, 0.36, 0.37, 0.38, 0.39, 0.40, 0.41, 0.42) \mu\text{m}$ .

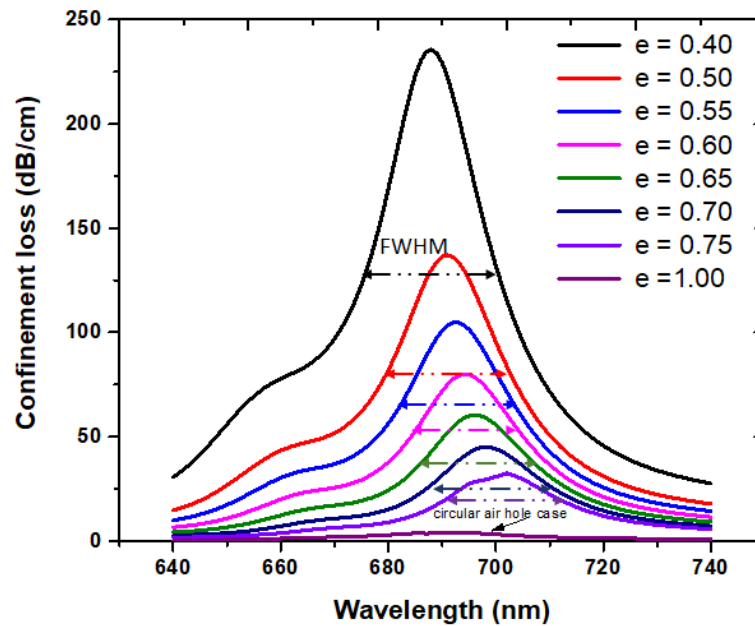


Figure 8. Confinement loss spectra of the core-guided mode for ellipticity ( $e = 0.40, 0.50, 0.55, 0.60, 0.65, 0.70, 0.75, \text{ and } 1.00$ ).

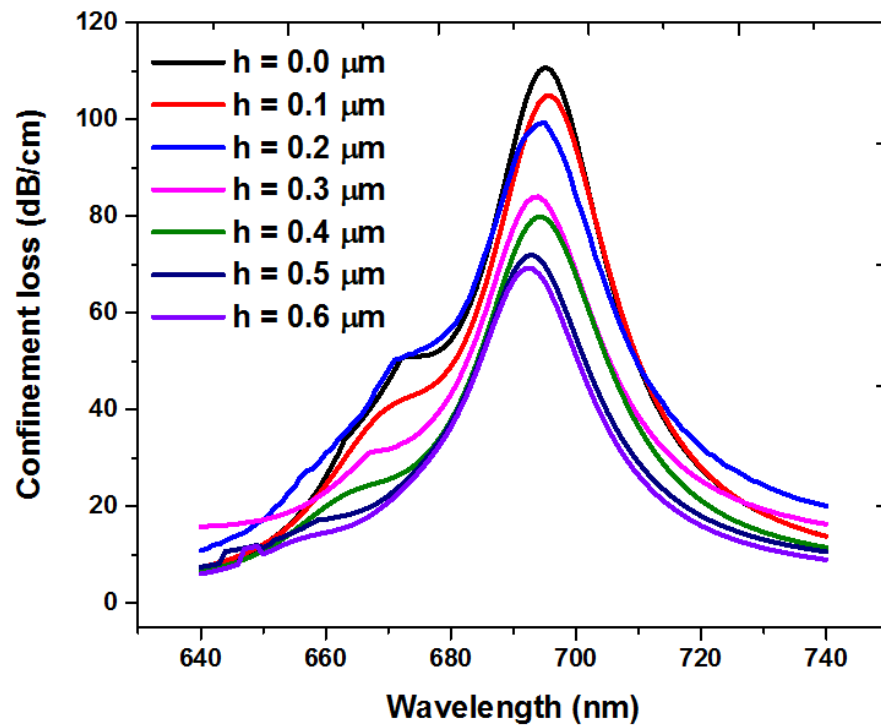


Figure 9. Confinement loss spectra of the core-guided mode for the distance between the top elliptical air hole and the flat surface ( $h = 0.1, 0.2, 0.3, 0.4, 0.5,$  and  $0.6 \mu\text{m}$ ).

#### 4. Application as a Refractive Index SPR-PCF Sensor

Finally, the application of the RI sensor based on the optimized designed structure was inspected. Table 4 shows the optimal geometrical parameters of the designed SPR-PCF based on the optimization of the structural parameters mentioned above.

Table 4. Optimal geometrical parameters of the proposed SPR-PCF.

$a_{1x}$ ( $\mu\text{m}$ )	$a_{1y}$ ( $\mu\text{m}$ )	$a_{2x}$ ( $\mu\text{m}$ )	$a_{2y}$ ( $\mu\text{m}$ )	$a_{3x}$ ( $\mu\text{m}$ )	$a_{3y}$ ( $\mu\text{m}$ )	$e$	$t_{Au}$ (nm)	$h$ ( $\mu\text{m}$ )
0.7e	0.7	0.78e	0.78	0.35e	0.35	0.55	30	0.4

Note:  $e$  is ellipticity.

To achieve precise RI detection, we examined the RI of the analyte,  $n_{ana} = 1.31, 1.32, 1.33, 1.34, 1.35, 1.36, 1.37, 1.38, 1.39, 1.391, 1.392, 1.393$  and  $1.395$ , as the surrounding media. Figure 10a,b present the CL spectra of the core-guided mode for the different RIs of analytes ( $n_{ana}$ ). Figure 10a illustrates  $n_{ana} = 1.31$ – $1.36$  in the step of  $0.01$ , and Figure 10b exhibits  $n_{ana} = 1.37, 1.38, 1.39, 1.391, 1.392, 1.393,$  and  $1.395$ . Note that the CL spectrum increases precipitously when the RI is in the range of  $1.39$ – $1.395$  due to the abrupt change of resonance condition between the core-guided mode and SPP mode. These results are similar to other studies (see [61–63]). We can explain this phenomenon in that the CL is proportional to  $\text{Im}(n_{eff})$ . The maximum  $n_{ana}$  value of  $1.395$  is chosen since there is no valid CL peak in the proposed structure when  $n_{ana} \geq 1.395$ , i.e., for target analyte  $\text{RI} \geq 1.3950$ , the  $\lambda_{peak}$  was not obtained, and consequently the overall sensitivity reduces. As observed in Figure 10a,b, all curves experience a redshift with an increase in  $n_{ana}$ . The positions of the CL peaks change slowly for a smaller value of  $n_{ana}$ ; e.g., CL peaks vary from  $25 \text{ dB/cm}$  to  $132 \text{ dB/cm}$  as  $n_{ana}$  increases from  $1.31$  to  $1.36$  in the step of  $0.01$ . Meanwhile, the positions of the CL peaks change rapidly with a higher value of  $n_{ana}$ , e.g., CL peaks vary from  $252 \text{ dB/cm}$  to  $3122 \text{ dB/cm}$  as  $n_{ana}$  rises from  $1.37, 1.38, 1.39, 1.391, 1.392, 1.393$  to  $1.395$ . Note that the CL spectrum displays a significant redshift when  $n_{ana} \geq 1.37$  (see Figure 10b). Remarkably, the designed SPR-PCF is susceptible to minimal variations in RI in the order of  $\pm 0.001$ .

One of the critical findings of the proposed SPR-PCF sensor is that it can detect the RI of the analyte higher than that of the fiber background.

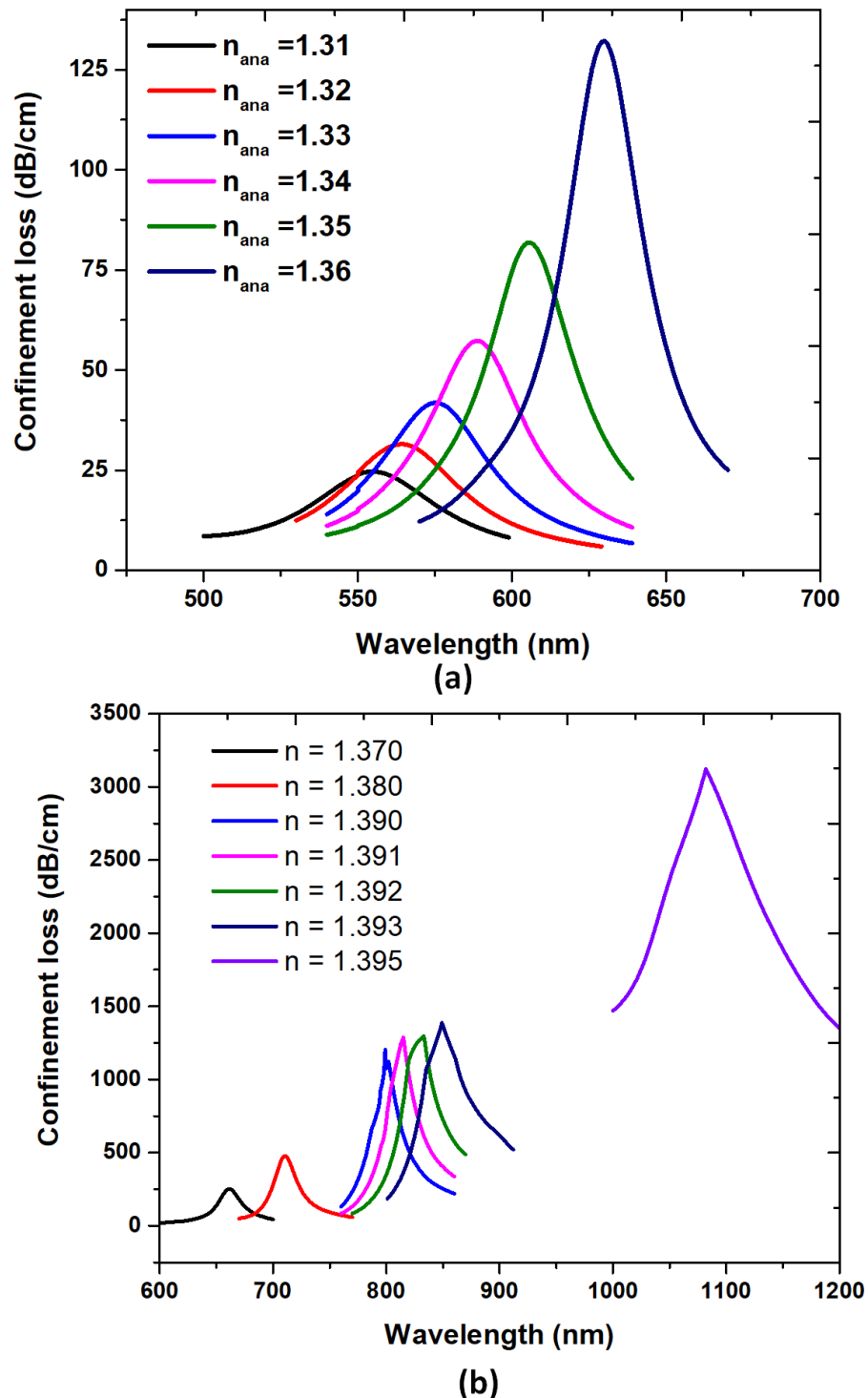


**Figure 10.** Confinement loss spectra of the core-guided mode for different RIs of analytes ( $n_{ana}$ ), (a)  $n_{ana} = 1.31, 1.32, 1.33, 1.34$  and  $1.35$  and (b)  $n_{ana} = 1.36, 1.37, 1.38, 1.39, 1.391, 1.392, 1.393$  and  $1.395$ .

Various RIs can be obtained in the wavelength interrogation mode by calculating the  $\Delta\lambda_{peak}$ . Figure 11 plots  $\lambda_{peak}$  and CL spectra of the core-guided mode for different analytes ( $n_{ana}$ ) ranging from 1.31–1.3950. The RI sensitivity  $S$  can be attained from Equation (4). As can be seen in Figure 11, the RI sensitivity  $S$  of the two adjacent points is  $S_{AB} = 116,500 \text{ nm/RIU}$ ,  $S_{BC} = 16,000 \text{ nm/RIU}$ ,  $S_{CD} = 18,000 \text{ nm/RIU}$ ,  $S_{DE} = 16,000 \text{ nm/RIU}$ ,

$S_{EF} = 8800 \text{ nm/RIU}$ ,  $S_{FG} = 5100 \text{ nm/RIU}$ ,  $S_{GH} = 3100 \text{ nm/RIU}$ ,  $S_{HI} = 2400 \text{ nm/RIU}$ ,  $S_{IJ} = 1700 \text{ nm/RIU}$ ,  $S_{JK} = 1300 \text{ nm/RIU}$ ,  $S_{KL} = 1100 \text{ nm/RIU}$ , and  $S_{LM} = 1100 \text{ nm/RIU}$ , corresponding to the wavelength interval of 550 nm to 1200 nm. The proposed SPR-PCF sensor's RI resolution can be obtained from Equation (5). The  $\Delta n_{ana}$  and  $\Delta \lambda_{peak}$  in  $S_{AB}$  shown in Figure 11 are  $\Delta n_{ana} = 0.002$  and  $\Delta \lambda_{peak} = 233 \text{ nm}$ , respectively. We assume  $\Delta \lambda_{min} = 0.1 \text{ nm}$ . Consequently, the minimum resolution can be obtained:  $8.58 \times 10^{-7} \text{ RIU}$ .

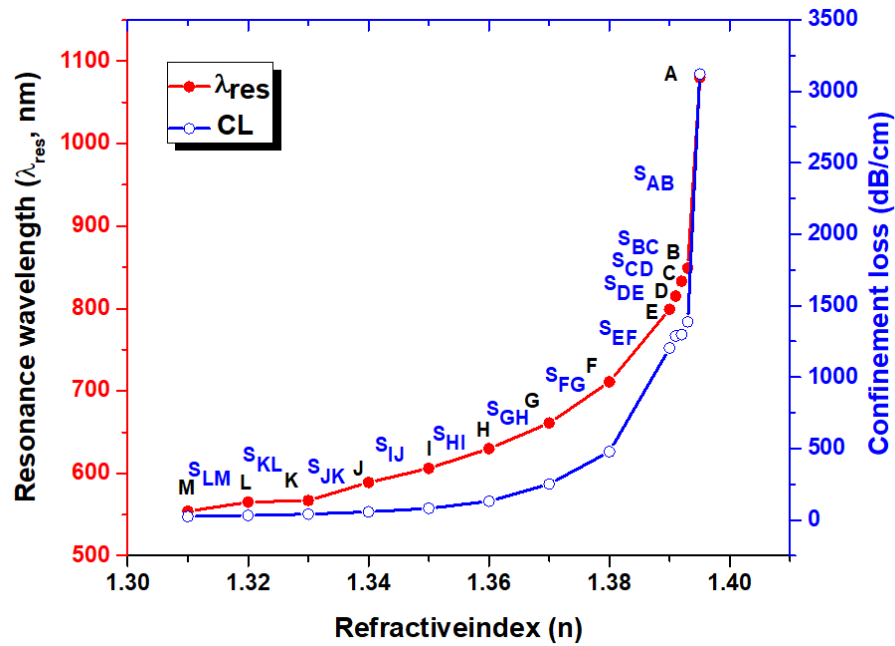


**Figure 11.** Resonance wavelength (nm) and confinement loss spectra of the core-guided mode for different analytes ( $n_{ana}$ ) ranging from 1.31 to 1.3950.

Concerning the performance of the proposed SPR-PCF, Table 5 contains the required data from Figure 11, including  $n_{ana}$ , CL (dB/cm),  $\lambda_{peak}$  (nm), sensor length (cm, based on Equation (6)), sensitivity (nm/RIU), and resolution (RIU), concerning the variation of RIs in the interval of 1.31–1.395.

**Table 5.** Observation of the performance of the designed SPR-PCF sensor for variation of RIs in the interval of 1.31–1.395.

$n_{ana}$	CL (dB/cm)	$\lambda_{peak}$ (cm)	Sensor Length (cm)	Sensitivity (nm/RIU)	Resolution (RIU)
1.31	24.62	554	0.0406	1100	$9.0909 \times 10^{-5}$
1.32	31.55	565	0.0316	1100	$9.0909 \times 10^{-5}$
1.33	41.78	576	0.0239	1300	$7.6923 \times 10^{-5}$
1.34	57.31	589	0.01744	1700	$5.8823 \times 10^{-5}$
1.35	81.86	606	0.01221	2400	$4.1667 \times 10^{-5}$
1.36	132.2	630	0.00756	3100	$3.2258 \times 10^{-5}$
1.37	252.34	661	0.00396	5000	$2.0000 \times 10^{-5}$
1.38	478.11	711	0.00209	8800	$1.1363 \times 10^{-5}$
1.39	1205.00	799	0.00083	16,000	$5.8823 \times 10^{-5}$
1.391	1288.20	815	0.00078	18,000	$5.56 \times 10^{-6}$
1.392	1297.90	833	0.00077	16,000	$6.25 \times 10^{-6}$
1.393	1367.00	849	0.00073	116,500	$8.58 \times 10^{-7}$
1.395	3121.80	1082	0.00032	N/A	N/A

Table 6 summarizes the performance analysis comparison (including published year, RI range, wavelength range, maximum wavelength sensitivity, and sensor resolution) between the proposed SPR-PCF sensor and previously reported sensors. Table 6 shows that our proposed SPR-PCF sensor reveals better sensing performance with higher sensitivity and better resolution.

**Table 6.** Performance analysis comparison between the proposed SPR-PCF sensor and previously reported sensors.

Refs./Year	RI Range	Wavelength Range (nm)	Max. Sensitivity (nm RIU <sup>-1</sup> )	Resolution (RIU)
[64]/2017	1.32–1.35	650–850	5600	$9.650 \times 10^{-6}$
[65]/2018	1.40–1.43	904–1359	15,180	$5.600 \times 10^{-6}$
[66]/2019	1.414–1.424	1900–2200	50,000	$4.000 \times 10^{-4}$
[67]/2020	1.39–1.43	650–1400	21,200	$4.720 \times 10^{-6}$
[68]/2020	1.33–1.36	400–800	3083	$3.200 \times 10^{-5}$
[69]/2021	1.35–1.50	1800–2200	4000	$2.940 \times 10^{-5}$
[70]/2021	1.43–1.49	900–1250	12,719	$7.460 \times 10^{-6}$
[41]/2022	1.33–1.39	600–960	13,000	$1.075 \times 10^{-6}$
[71]/2022	1.30–1.44	800–1100	1100	$9.090 \times 10^{-6}$
This work	1.31–1.3950	550–1200	116,500	$8.58 \times 10^{-7}$

## 5. Conclusions

In summary, we designed a simple and high-sensitivity elliptical air hole SPR-PCF-based sensor where Au is deposited as a plasmonic material to deploy an external sensing approach. We used FEM-based COMSOL Multiphysics software to simulate the sensor and further characterize the performance. Through FEM simulations, the influences of RI on structural parameters of the SPR-PCF were discussed and calculated. We found that the thickness of plasmonic material (Au) is the most important factor affecting the FWHM and CL amplitude. We also demonstrated that the proposed elliptical air hole SPR-PCF is superior to the circular air hole SPR-PCF based on CL and FWHM. Under the optimized structural parameters, the proposed SPR-PCF sensor verifies the highest wavelength sensitivity of 116,500 nm/RIU with an  $8.58 \times 10^{-7}$  RIU sensing solution for the analyte RI of 1.395. The device can detect highly active chemical and biological liquid samples because of its excellent sensing performance.

**Author Contributions:** Conceptualization, investigation, C.-T.C.C.; methodology, software, and data curation, M.R.R.K.; validation, formal analysis, resources R.T.; writing—original draft preparation, C.-T.C.C.; writing—review and editing, Y.-F.C.C. All authors have read and agreed to the published version of the manuscript.

**Funding:** This research was funded by the University Research Grant of Universiti Brunei Darussalam, grant number UBD/RSCH/1.9/FICBF(b)/2022/018.

**Institutional Review Board Statement:** Not applicable.

**Informed Consent Statement:** Not applicable.

**Data Availability Statement:** Not applicable.

**Acknowledgments:** The authors thankfully acknowledge the financial support rendered by the Universiti Brunei Darussalam.

**Conflicts of Interest:** The authors declare no conflict of interest.

## References

1. Chau, Y.-F.; Yeh, H.-H.; Tsai, D. Surface plasmon resonances effects on different patterns of solid-silver and silver-shell nanocylindrical pairs. *J. Electromagn. Waves Appl.* **2010**, *24*, 1005–1014. [[CrossRef](#)]
2. Deng, Y.; Cao, G.; Yang, H.; Zhou, X.; Wu, Y. Dynamic Control of Double Plasmon-Induced Transparencies in Aperture-Coupled Waveguide-Cavity System. *Plasmonics* **2018**, *13*, 345–352. [[CrossRef](#)]
3. Deng, Y.; Cao, G.; Wu, Y.; Zhou, X.; Liao, W. Theoretical Description of Dynamic Transmission Characteristics in MDM Waveguide Aperture-Side-Coupled with Ring Cavity. *Plasmonics* **2015**, *10*, 1537–1543. [[CrossRef](#)]
4. Lin, C.-T.; Chang, M.-N.; Huang, H.J.; Chen, C.-H.; Sun, R.-J.; Liao, B.-H.; Chau, Y.-F.C.; Hsiao, C.-N.; Shiao, M.-H.; Tseng, F.-G. Rapid fabrication of three-dimensional gold dendritic nanoforests for visible light-enhanced methanol oxidation. *Electrochim. Acta* **2016**, *192*, 15–21. [[CrossRef](#)]
5. Hsieh, L.-Z.; Chau, Y.-F.C.; Lim, C.M.; Lin, M.-H.; Huang, H.J.; Lin, C.-T.; Syafi'ie, I.M.N. Metal nano-particles sizing by thermal annealing for the enhancement of surface plasmon effects in thin-film solar cells application. *Opt. Commun.* **2016**, *370*, 85–90. [[CrossRef](#)]

6. Chau, Y.-F.; Jiang, Z.-H.; Li, H.-Y.; Lin, G.-M.; Wu, F.-L.; Lin, W.-H. Localized resonance of composite core-shell nanospheres, nanobars and nanospherical chains. *Prog. Electromagn. Res. B* **2011**, *28*, 183–199. [[CrossRef](#)]
7. Divya, J.; Selvendran, S.; Raja, A.S.; Sivasubramanian, A. Surface plasmon based plasmonic sensors: A review on their past, present and future. *Biosens. Bioelectron. X* **2022**, *11*, 100175. [[CrossRef](#)]
8. Shangguan, Q.; Chen, Z.; Yang, H.; Cheng, S.; Yang, W.; Yi, Z.; Wu, X.; Wang, S.; Yi, Y.; Wu, P. Design of Ultra-Narrow Band Graphene Refractive Index Sensor. *Sensors* **2022**, *22*, 6483. [[CrossRef](#)]
9. Chen, H.; Chen, Z.; Yang, H.; Wen, L.; Yi, Z.; Zhou, Z.; Dai, B.; Zhang, J.; Wu, X.; Wu, P. Multi-mode surface plasmon resonance absorber based on dart-type single-layer graphene. *RSC Adv.* **2022**, *12*, 7821–7829. [[CrossRef](#)]
10. Liedberg, B.; Nylander, C.I.; Lunström, I. Surface plasmon resonance for gas detection and biosensing. *Sens. Actuators B Chem.* **1983**, *4*, 299–304. [[CrossRef](#)]
11. Jorgenson, R.C.; Yee, S.S. A fiber-optic chemical sensor based on surface plasmon resonance. *Sens. Actuators B Chem.* **1993**, *12*, 213–220. [[CrossRef](#)]
12. Nazeri, K.; Bradley, C. The effect of photonic crystal fibre structure on the performance of Mach-Zehnder interferometer fibre optic gas sensors. *Opt. Fiber Technol.* **2020**, *58*, 102294. [[CrossRef](#)]
13. Kim, H.; Kim, J.; Paek, U.-C.; Lee, B.H.; Kim, K.T. Tunable photonic crystal fiber coupler based on a side-polishing technique. *Opt. Lett.* **2004**, *29*, 1194–1196. [[CrossRef](#)]
14. Tan, Y.C.; Tou, Z.Q.; Chow, K.K.; Chan, C.C. Graphene-deposited photonic crystal fibers for continuous refractive index sensing applications. *Opt. Express* **2015**, *23*, 31286–31294. [[CrossRef](#)] [[PubMed](#)]
15. Paul, A.K.; Habib, S.; Hai, N.H.; Razzak, S.A. An air-core photonic crystal fiber based plasmonic sensor for high refractive index sensing. *Opt. Commun.* **2020**, *464*, 125556. [[CrossRef](#)]
16. Gupta, A.; Singh, H.; Singh, A.; Singh, R.K.; Tiwari, A. D-Shaped Photonic Crystal Fiber-Based Surface Plasmon Resonance Biosensors with Spatially Distributed Bimetallic Layers. *Plasmonics* **2020**, *15*, 1323–1330. [[CrossRef](#)]
17. Han, B.; Zhang, Y.-N.; Siyu, E.; Wang, X.; Yang, D.; Wang, T.; Lu, K.; Wang, F. Simultaneous measurement of temperature and strain based on dual SPR effect in PCF. *Opt. Laser Technol.* **2019**, *113*, 46–51. [[CrossRef](#)]
18. Xie, Q.; Chen, Y.; Li, X.; Yin, Z.; Wang, L.; Geng, Y.; Hong, X. Characteristics of D-shaped photonic crystal fiber surface plasmon resonance sensors with different side-polished lengths. *Appl. Opt.* **2017**, *56*, 1550–1555. [[CrossRef](#)]
19. Chau, Y.-F.; Liu, C.-Y.; Yeh, H.-H.; Tsai, D.P. A comparative study of high birefringence and low confinement loss photonic crystal fiber employing elliptical air holes in fiber cladding with tetragonal lattice. *Prog. Electromagn. Res. B* **2010**, *22*, 39–52. [[CrossRef](#)]
20. Wu, T.; Shao, Y.; Wang, Y.; Cao, S.; Cao, W.; Zhang, F.; Liao, C.; He, J.; Huang, Y.; Hou, M.; et al. Surface plasmon resonance biosensor based on gold-coated side-polished hexagonal structure photonic crystal fiber. *Opt. Express* **2017**, *25*, 20313–20322. [[CrossRef](#)] [[PubMed](#)]
21. Xiang, H.; Jiang, Y. Fiber Bragg grating inscription in multi-core photonic crystal fiber by femtosecond laser. *Optik* **2018**, *171*, 9–14. [[CrossRef](#)]
22. Haider, F.; Aoni, R.A.; Ahmed, R.; Miroshnichenko, A.E. Highly amplitude-sensitive photonic-crystal-fiber-based plasmonic sensor. *J. Opt. Soc. Am. B* **2018**, *35*, 2816–2821. [[CrossRef](#)]
23. Popescu, V.; Sharma, A.K.; Marques, C. Resonant interaction between a core mode and two complementary supermodes in a honeycomb PCF reflector-based SPR sensor. *Optik* **2021**, *227*, 166121. [[CrossRef](#)]
24. Tong, K.; Wang, F.; Wang, M.; Dang, P.; Wang, Y. Three-core photonic crystal fiber surface plasmon resonance sensor. *Opt. Fiber Technol.* **2018**, *46*, 306–310. [[CrossRef](#)]
25. Wang, D.; Yi, Z.; Ma, G.; Dai, B.; Yang, J.; Zhang, J.; Yu, Y.; Liu, C.; Wu, X.; Bian, Q. Two-channel photonic crystal fiber based on surface plasmon resonance for magnetic field and temperature dual-parameter sensing. *Phys. Chem. Chem. Phys.* **2022**, *24*, 21233–21241. [[CrossRef](#)]
26. Yan, X.; Wang, Y.; Cheng, T.; Li, S. Photonic Crystal Fiber SPR Liquid Sensor Based on Elliptical Detective Channel. *Micromachines* **2021**, *12*, 408. [[CrossRef](#)] [[PubMed](#)]
27. Islam, M.R.; Iftekher, A.N.M.; Hasan, K.R.; Nayen, J.; Islam, S.B.; Hossain, A.; Mustafa, Z.; Tahsin, T. Design and numerical analysis of a gold-coated photonic crystal fiber based refractive index sensor. *Opt. Quantum Electron.* **2021**, *53*, 112. [[CrossRef](#)]
28. Gao, D.; Guan, C.; Wen, Y.; Zhong, X.; Yuan, L. Multi-hole fiber based surface plasmon resonance sensor operated at near-infrared wavelengths. *Opt. Commun.* **2014**, *313*, 94–98. [[CrossRef](#)]
29. Han, H.; Hou, D.; Luan, N.; Bai, Z.; Song, L.; Liu, J.; Hu, Y. Surface Plasmon Resonance Sensor Based on Dual-Side Polished Microstructured Optical Fiber with Dual-Core. *Sensors* **2020**, *20*, 3911. [[CrossRef](#)]
30. Wang, Q.; Zhang, X.; Yan, X.; Wang, F.; Cheng, T. Design of a Surface Plasmon Resonance Temperature Sensor with Multi-Wavebands Based on Conjoined-Tubular Anti-Resonance Fiber. *Photonics* **2021**, *8*, 231. [[CrossRef](#)]
31. Wang, Y.; Huang, Q.; Zhu, W.; Yang, M.; Lewis, E. Novel optical fiber SPR temperature sensor based on MMF-PCF-MMF structure and gold-PDMS film: Erratum. *Opt. Express* **2019**, *27*, 10813. [[CrossRef](#)] [[PubMed](#)]
32. Rafi, H.N.; Kaysir, R.; Islam, J. Air-hole attributed performance of photonic crystal fiber-based SPR sensors. *Sens. Bio-Sens. Res.* **2020**, *29*, 100364. [[CrossRef](#)]
33. Rahman, K.M.; Alam, M.S.; Islam, M.A. Highly sensitive gold-coated surface plasmon resonance photonic crystal fiber sensor in near-infrared region. *Results Opt.* **2022**, *7*, 100223. [[CrossRef](#)]

34. Zhou, X.; Cheng, T.; Li, S.; Suzuki, T.; Ohishi, Y. Practical sensing approach based on surface plasmon resonance in a photonic crystal fiber. *OSA Contin.* **2018**, *1*, 1332–1340. [[CrossRef](#)]
35. Kamrunnahar, Q.M.; Haider, F.; Aoni, R.A.; Mou, J.R.; Shifa, S.; Begum, F.; Abdul-Rashid, H.A.; Ahmed, R. Plasmonic Micro-Channel Assisted Photonic Crystal Fiber Based Highly Sensitive Sensor for Multi-Analyte Detection. *Nanomaterials* **2022**, *12*, 1444. [[CrossRef](#)] [[PubMed](#)]
36. Liu, Q.; Li, S.; Gao, X. Highly sensitive plasmonics temperature sensor based on photonic crystal fiber with a liquid core. *Opt. Commun.* **2018**, *427*, 622–627. [[CrossRef](#)]
37. Liang, H.; Shen, T.; Feng, Y.; Xia, Z.; Liu, H. A Surface Plasmon Resonance Temperature Sensing Unit Based on a Graphene Oxide Composite Photonic Crystal Fiber. *IEEE Photonics J.* **2020**, *12*, 1–11. [[CrossRef](#)]
38. Shakya, A.K.; Singh, S. Design of novel Penta core PCF SPR RI sensor based on fusion of IMD and EMD techniques for analysis of water and transformer oil. *Measurement* **2022**, *188*, 110513. [[CrossRef](#)]
39. Kiroriwal, M.; Singal, P. Design and analysis of highly sensitive solid core gold-coated hexagonal photonic crystal fiber sensor based on surface plasmon resonance. *J. Nanophotonics* **2021**, *15*, 026008. [[CrossRef](#)]
40. Shakya, A.K.; Singh, S. Design of dual polarized tetra core PCF based plasmonic RI sensor for visible-IR spectrum. *Opt. Commun.* **2021**, *478*, 126372. [[CrossRef](#)]
41. Kumar, A.; Verma, P.; Jindal, P. Surface plasmon resonance biosensor based on a D-shaped photonic crystal fiber using Ti3C2Tx MXene material. *Opt. Mater.* **2022**, *128*, 112397. [[CrossRef](#)]
42. Paul, A.K.; Sarkar, A.K.; Islam, H.; Morshed, M. Dual core photonic crystal fiber based surface plasmon resonance biosensor. *Optik* **2018**, *170*, 400–408. [[CrossRef](#)]
43. Zhao, Y.; Deng, Z.-Q.; Li, J. Photonic crystal fiber based surface plasmon resonance chemical sensors. *Sens. Actuators B Chem.* **2014**, *202*, 557–567. [[CrossRef](#)]
44. Yasli, A.; Ademgil, H. Effect of plasmonic materials on photonic crystal fiber based surface plasmon resonance sensors. *Mod. Phys. Lett. B* **2019**, *33*, 1950157. [[CrossRef](#)]
45. Steel, M.J.; Osgood, R.M. Elliptical-hole photonic crystal fibers. *Opt. Lett.* **2001**, *26*, 229–231. [[CrossRef](#)] [[PubMed](#)]
46. Sun, Y.-S.; Chau, Y.-F.; Yeh, H.-H.; Tsai, D.P. Highly birefringent index-guiding photonic crystal fiber with squeezed differently sized air-holes in cladding. *Jpn. J. Appl. Phys.* **2008**, *47*, 3755. [[CrossRef](#)]
47. Chau, Y.-F.; Yeh, H.-H.; Tsai, D.P. Significantly enhanced birefringence of photonic crystal fiber using rotational binary unit cell in fiber cladding. *Jpn. J. Appl. Phys.* **2007**, *46*, L1048. [[CrossRef](#)]
48. Yang, K.-Y.; Chau, Y.-F.; Huang, Y.-W.; Yeh, H.-Y.; Tsai, D.P. Design of high birefringence and low confinement loss photonic crystal fibers with five rings hexagonal and octagonal symmetry air-holes in fiber cladding. *J. Appl. Phys.* **2011**, *109*, 093103. [[CrossRef](#)]
49. Chau, Y.-F.; Yeh, H.-H.; Tsai, D.P. A New Type of Optical Antenna: Plasmonics Nanoshell Bowtie Antenna with Dielectric Hole. *J. Electromagn. Waves Appl.* **2010**, *24*, 1621–1632. [[CrossRef](#)]
50. Chau, Y.-F.C. Mid-infrared sensing properties of a plasmonic metal–insulator–metal waveguide with a single stub including defects. *J. Phys. D Appl. Phys.* **2020**, *53*, 115401. [[CrossRef](#)]
51. Wang, D.; Zhu, W.; Yi, Z.; Ma, G.; Xiang, G.; Dai, B.; Yu, Y.; Zhou, G.; Wu, P.; Liu, C. Highly sensitive sensing of a magnetic field and temperature based on two open ring channels SPR-PCF. *Opt. Express* **2022**, *30*, 39055–39067. [[CrossRef](#)]
52. Isti, M.I.A.; Talukder, H.; Islam, S.M.R.; Nuzhat, S.; Hosen, A.S.M.S.; Cho, G.H.; Biswas, S.K. Asymmetrical D-channel photonic crystal fiber-based plasmonic sensor using the wavelength interrogation and lower birefringence peak method. *Results Phys.* **2020**, *19*, 103372. [[CrossRef](#)]
53. Chen, Y.; Xie, Q.; Li, X.; Zhou, H.; Hong, X.; Geng, Y. Experimental realization of D-shaped photonic crystal fiber SPR sensor. *J. Phys. D Appl. Phys.* **2017**, *50*, 025101. [[CrossRef](#)]
54. Al Mahfuz, M.; Hasan, R.; Momota, M.R.; Masud, A.; Akter, S. Asymmetrical photonic crystal fiber based plasmonic sensor using the lower birefringence peak method. *OSA Contin.* **2019**, *2*, 1713–1725. [[CrossRef](#)]
55. Boyd, D.A.; Greengard, L.; Brongersma, M.; El-Naggar, M.Y.; Goodwin, D.G. Plasmon-assisted chemical vapor deposition. *Nano Lett.* **2006**, *6*, 2592–2597. [[CrossRef](#)] [[PubMed](#)]
56. Lv, J.; Liang, T.; Gu, Q.; Liu, Q.; Ying, Y.; Si, G. A High Refractive Index Plasmonic Micro-Channel Sensor Based on Photonic Crystal Fiber. *Nanomaterials* **2022**, *12*, 3764. [[CrossRef](#)] [[PubMed](#)]
57. Guiyao, Z.; Zhiyun, H.; Shuguang, L.; Lantian, H. Fabrication of glass photonic crystal fibers with a die-cast process. *Appl. Opt.* **2006**, *45*, 4433–4436. [[CrossRef](#)] [[PubMed](#)]
58. Issa, N.A.; van Eijkelenborg, M.A.; Fellew, M.; Cox, F.; Henry, G.; Large, M.C.J. Fabrication and study of microstructured optical fibers with elliptical holes. *Opt. Lett.* **2004**, *29*, 1336–1338. [[CrossRef](#)]
59. Beltrán-Mejía, F.; Chesini, G.; Silvestre, E.; George, A.K.; Knight, J.C.; Cordeiro, C.M. Ultrahigh-birefringent squeezed lattice photonic crystal fiber with rotated elliptical air holes. *Opt. Lett.* **2010**, *35*, 544–546. [[CrossRef](#)]
60. Zha, F.; Li, J.; Sun, P.; Ma, H. Highly sensitive selectively coated D-shape photonic crystal fibers for surface plasmon resonance sensing. *Phys. Lett. A* **2019**, *383*, 1825–1830. [[CrossRef](#)]
61. Wang, S.; Lu, Y.; Ma, W.; Liu, N.; Fan, S. D-Shaped Surface Plasmon Photonic Crystal Fiber Temperature Sensor. *Plasmonics* **2022**, *17*, 1911–1919. [[CrossRef](#)]

62. Zuhayer, A.; Shafkat, A. Design and analysis of a gold-coated dual-core photonic crystal fiber bio-sensor using surface plasmon resonance. *Sens. Bio.-Sens. Res.* **2021**, *33*, 100432. [[CrossRef](#)]
63. Akter, S.; Rahman, Z.; Mahmud, S. Highly sensitive open-channels based plasmonic biosensor in visible to near-infrared wavelength. *Results Phys.* **2019**, *13*, 102328. [[CrossRef](#)]
64. An, G.; Hao, X.; Li, S.; Yan, X.; Zhang, X. D-shaped photonic crystal fiber refractive index sensor based on surface plasmon resonance. *Appl. Opt.* **2017**, *56*, 6988–6992. [[CrossRef](#)]
65. Lu, J.; Li, Y.; Han, Y.; Liu, Y.; Gao, J. D-shaped photonic crystal fiber plasmonic refractive index sensor based on gold grating. *Appl. Opt.* **2018**, *57*, 5268–5272. [[CrossRef](#)] [[PubMed](#)]
66. Thenmozhi, H.; Rajan, M.S.M.; Ahmed, K. D-shaped PCF sensor based on SPR for the detection of carcinogenic agents in food and cosmetics. *Optik* **2019**, *180*, 264–270. [[CrossRef](#)]
67. Fu, Y.; Liu, M.; Shum, P.; Chu, L. An ultrahighly sensitive photonic crystal fiber based surface plasmon resonance sensor. *Optik* **2020**, *212*, 164649. [[CrossRef](#)]
68. Yasli, A.; Ademgil, H.; Haxha, S.; Aggoun, A. Multi-Channel Photonic Crystal Fiber Based Surface Plasmon Resonance Sensor for Multi-Analyte Sensing. *IEEE Photonics J.* **2020**, *12*, 1–15. [[CrossRef](#)]
69. Chu, S.; Nakkeeran, K.; Abobaker, A.M.; Aphale, S.S.; Sivabalan, S.; Babu, P.R.; Senthilnathan, K. A surface plasmon resonance bio-sensor based on dual core D-shaped photonic crystal fibre embedded with silver nanowires for multisensing. *IEEE Sens. J.* **2020**, *21*, 76–84. [[CrossRef](#)]
70. Yan, X.; Fu, R.; Cheng, T.; Li, S. A Highly Sensitive Refractive Index Sensor Based on a V-Shaped Photonic Crystal Fiber with a High Refractive Index Range. *Sensors* **2021**, *21*, 3782. [[CrossRef](#)]
71. Rahman, A.; Ahmed, T.; Haque, I.; Anower, S. A Photonic Crystal Fiber Based Asymmetric Slotted Structured Highly Sensitive Refractive Index Plasmonic Biosensor. *J. Sens. Technol.* **2022**, *12*, 1–17. [[CrossRef](#)]